International Journal of Thermofluids 24 (2024) 100853

Contents lists available at ScienceDirect

International Journal of Thermofluids

journal homepage: www.sciencedirect.com/journal/international-journal-of-thermofluids

Simulation and design of a solar chimney integrated with phase change material layer for building ventilation

Hussam Hakeem Qasim [a,*], Ahmed K. Alshara [b], Falah A. Abood [a]

[a] Department of Mechanical Engineering, College of Engineering, University of Basrah, Basrah, Iraq
[b] Department of Mechanical Engineering, College of Engineering, University of Misan, Misan, Iraq

ARTICLE INFO

Keywords:
Solar chimney
Phase change material (PCM)
Ventilation
Air change per hour (ACH)

ABSTRACT

The development of modern life requires new energy sources, and one of this energy is renewable solar energy uses in solar chimney for natural ventilation, but at the present time it is not greatly invested, taking into account the weather conditions of the region and the physical characteristics of solar radiation and air in the area in which the study will be conducted. The current study was carried out in Basrah city- Iraq, at longitude 47.749° and latitude 30.568°, where the solar chimney was facing south. The investigation was conducted using both theoretical and experimental studied. In the theoretical study, the solar chimney with the room in the presence and absence of PCM was simulated numerically using the finite volume method using the soft package ANSYS-Fluent/2021/R2. The effect of different tilt angles (α = 30°, 45°, and 60°), solar chimney air gap (gab = 10 cm, 15 cm, and 20 cm), and PCM basin thickness (t_{PCM} = 3 cm, 4 cm, and 5 cm) were investigated. The results were presented in the form of contours of the distribution of streamlines, velocity, temperature, and liquid fraction of the solar chimney with the room, rate of temperature of the absorber plate with time and the rate of temperature of the PCM (T_{PCM}) with time, rate of air change per hour (ACH). As for the experimental side, the device was built, and the intensity of solar radiation was studied for several days on 30 Sep. and 15 Oct. 2023, the temperature distribution rate of the absorbent plate over time, the PCM temperature rate, and the air change per hour (ACH). The theoretical results were compared with the experimental results, where there was good agreement, and the theoretical comparison was also made with several researchers. Significant results showed that the optimal ratio of the air gap width of the solar chimney is 15 cm, the inclination angle of the solar chimney α = 30°, and the thickness of the PCM basin (t_{PCM} = 4 cm) to obtain the maximum ventilation rate. The thickness of the PCM basin = 4 cm gives the largest liquid fraction along time and maximum average temperature of the absorber plate. On the experimental, it was found that PCM convert into the liquid phase after its melting point, which is 340 K, after 12 noon, and the highest value of ACH reached 37 on September 30/2023 at midday.

1. Introduction

Solar chimney is one of the recent technologies used to reduce consumption by utilizing solar energy as well as by using a phase change material (PCM) to store heat. Many factors affect the efficiency of the solar chimney, such as the size of the buildings, location of the inlet and outlet openings, insulation quality and type, absorber plate and method of coating it and its type, dimensions of the solar collector, the size of the solar collector, temperature, velocity and humidity of the outside air, solar radiation and the angle of incidence. As many researches have been showed on this topic. Studies continued for the performance of solar chimney for the models conducted on various investigated numerical and experimental applications. Finding that the most of the papers use several simulation programs to compare and support experimental results, this indicates that the method of simulating results is important for predicting and understanding the complex behavior of a solar chimney with phase change material.

Safari and Torabi [1] analyzed numerically the effect of the combination of solar thermal energy storage with solar passive heating. The integrated geometry was numerically analyzed in two different cases,

* Corresponding author.
E-mail addresses: pgs.hussam.hakeem@uobasrah.edu.iq (H.H. Qasim), dr.ahmed_alshara@uomisan.edu.iq (A.K. Alshara), falah.abood@uobasrah.edu.iq (F.A. Abood).

https://doi.org/10.1016/j.ijft.2024.100853

Available online 14 September 2024
2666-2027/© 2024 The Author(s). Published by Elsevier Ltd. This is an open access article under the CC BY license (http://creativecommons.org/licenses/by/4.0/).

with and without PCM. The results showed when using PCM, the temperature of the guardroom can be maintained, while without the use of PCM the room temperature varies during day and night. Li et al. [2] achieved numerically the thermal storage capacity and air flow rate of solar chimney combined with different PCMs during nighttime. The results expose that a lower PCM temperature can increase the chargeability hence discharge a solar chimney, in which a higher PCM temperature requires a higher solar radiation intensity and longest charging time for a solar chimney. Dordelly et al. [3] studied numerically and experimentally of a PCM with solar chimney in laboratory and in situ conditions. The results showed a slight improvement in performance in terms of mass flow rate, outside temperature and outlet temperature difference despite the incomplete integration of the PCM. During periods of low wind speed and surface temperatures exceeding 45 °C to activate the PCM panels, the flow rate increased by 11.3659 m^3/h. Buonomo et al. [4] investigated for two dimensional numerical solar chimneys with an absorbing capacity wall in a south facade of a building. The capacity wall is composed of a high absorbing plate and an assigned thickness of phase change material. The problem is solved by use the Ansys – Fluent program. Finding that the PCM is not completely liquid, but it is changing phase and its temperature increase is independent of the radiant energy. Salih et al. [5] used a mathematical model to analyze the forced convection turbulent flow in a novel solar air heater with multiple rectangular capsules filled with paraffin wax-based phase change material. The studied was conducted under three airflow velocities, and an average solar flux of 625 W/m^2. Findings revealed that raising airflow velocity during charging delayed the melting time and reduced the melting temperature of PCM. Nateghi and Jahangir [6] studied numerically the performance of solar chimney in providing thermal comfort by adding PCM. The results showed that the solar chimney with PCM is not suitable in hot and dry climate in both ventilation and heating, as the thermal comfort indicators changed from -0.16 to -0.31 (summer) and from 0.34 to 0.78 in (winter). The PCM can improve the performance of solar chimney and be better in winter or cold semi-arid climate when there is a large temperature difference between day and night. Nasr and Hammadi [7] investigated the impact of PCM and roof shading on the cooling load of a residential unit in Basrah, Iraq. Finding that the PCM installation on the outer surface of the wall and roof resulted in the highest reduction of cooling load of about 18 %. Roof shading, using corrugated galvanized iron, also it reduced heat gain from solar radiation, resulting in a cooling load reduction of approximately 5 %. Abduljabbar et al. [8] analyzed the performance of a two-story building with a vertical solar chimney using ANSYS 2022/R1. Results showed that the wax was enhancing air change per hour (ACH), indoor temperature, and ventilation period after sunset. The solar chimney integrated with energy storage extended the ventilation period after sunset. The ACH increased by 18.3 % and 9.98 % for the second floor, while indoor temperature decreased by 1.17 K and 0.68 K.

Qin et al. [9] investigated numerically and experimentally the system that integrates a conventional heat exchanger and a solar air heater with PCM. Experimental testing and numerical analysis were carried out using the volume control method to predict thermal and energy performance. The findings showed that the PCM can effectively stabilize the outlet air temperature in the range of (33 – 35.8) °C for nearly 4.5 h., reduce the peak outlet air temperature by 8 °C and increase the working period to 24 h. Tiji et al. [10] studied numerically for PCM with solar chimney and finned absorber. The simulation was carried out for a whole winter day, the results showed that the addition of PCM improves the uniformity of the room temperature, as they found that the average room temperature is 14.68 °C without fins, which is much lower than the thermal comfort condition, and the highest temperature uniformity occurred at 12 o'clock, where it was the value of 60 % which means that the average room temperature decreased by 30 % compared to the case without PCM. Liu et al. [11] studied numerically the thermal performance of phase change material (PCM) with earth – air heat exchanger (EAHE) as a passive technology without solar chimney. The results showed that the phase change temperature should be consistent with the ambient air temperature to maintain thermal balance and improve performance. The diameter of the PCM container had no effect on the thermal performance. Also, findings that at higher air velocities, the cooling/heating capacity improves, but lower air velocities are desirable. Long et al. [12] investigated numerically the solar chimney with an EAHE for passive ventilation system and the providing of fresh air and cooling capacity. The period of completely melted was approximately 5 h 15:30 to 20:30 and PCM solidified from 02:00 – 7:15. Added PCM to the system increased the airflow rate by 50 % at night and the maximum airflow rate decreased by 17.8 %. Maytorena et al. [13] studied numerically two passive technologies were combined into a room with a PCM-assisted rectangular earth – air heat exchanger (REAHE), suggested a room with a PCM on its roof which acts as a thermal insulator and reduction of peak heat flow into the ceiling by up to 33 %. Discovered that the best system is with the addition of PCM in the top of the room with a thickness between (1.5 – 2) cm, and the best type of PCM is RT35HC because it has low thermal diffusivity, high latent heat and high phase change temperature. The results also showed that the less mass of PCM, the faster the recovery occurs.

Thantong et al. [14] studied experimentally the thermal performance of the new solar chimney configuration incorporating a phase change material. This solar chimney with phase change material it consists of double walls with a 0.05 m air gap between the walls. Solar chimney with phase change material is integrated into the south face of the small house. The results indicated that the internal temperature of the solar chimney with PCM in the room was lower than the single concrete wall room. Fadaei et al. [15] investigated experimentally the effect of latent heat storage on solar chimney. Paraffin wax was used in the solar chimney as a phase change material. The results showed that the maximum absorber surface temperature for solar chimney with PCM is 72 °C and without PCM is 69 °C. The maximum velocity of air is 1.9 m/s, while it is 2 m/s without PCM, this means PCM causes an increase in average mass flow rate about 8.33 %. Hachim et al. [16] presented numerically and experimentally the effective working time of unglazed solar collectors which can be extended by using a double pass (descending and ascending) where air flows and energy is stored in a phase change material. The results showed that the performance of hybrid solar collectors does not depend on the diameter of the holes on the perforated plate and the vertical distance between the holes. The best thermal performance using PCM type RT27 and this applies to the almost stable radiation system. For the unstable radiation system, PCM type RT35 is used, as it gives good thermal performance during days when the sky is clear and the radiation system is stable.

From previous research, we note that the presence of a tank containing PCM materials and attached to the solar collector and subject to changing the angle of inclination of the solar collector, the thickness of the basin, and the height of the solar chimney channel have not been studied in depth. Therefore, the current study aims to study a solar chimney containing two-phase materials directly connected to a room and to know the most important variables that affect the air change rate ACH, such as the thickness of the PCM basin, the angle of inclination of the solar collector, and its height, by performing a simulation using the ANSYS – Fluent 2021/R2 program, as well as a practical design of a solar chimney with a room.

2. Materials and methods

2.1. Numerical analysis

2.1.1. Geometrical configuration

Different shapes of a models for the room with the solar chimney without PCM were conducted for solar chimney gab = 10 cm, 15 cm, and 20 cm and different tilt angle for solar chimney $\alpha = 30°$, 45°, and 60° and with inlet opening at the bottom of the room. And the model for adding

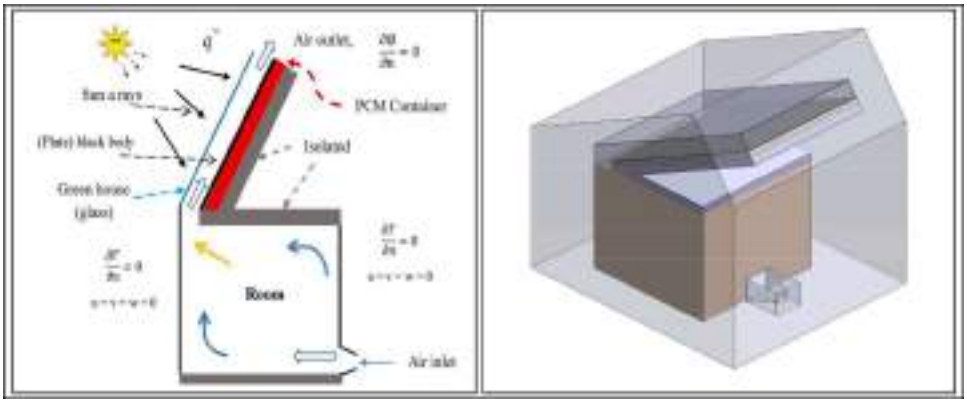

Fig. 1. Schematic of solar chimney with room (2-D) in the left and (3-D) in the right.

Table 1
The basic parameters and dimensions for the prototype models.

Basic parameter of the prototype	Value
Solar collector gap	0.1 m, 0.15 m, 0.2 m
Solar collector length	1.5 m
Solar collector width	1 m
Dimension of solar collector outlet	0.15 m × 1 m
Glass thickness (t_g)	4 mm
Area of solar collector roof	1.5 m^2
Aluminium plate sheet length (L_{AS})	1.5 m
Aluminium plate sheet width (w_{AS})	1 m
Aluminium plate sheet thickness (t_{AS})	1 mm
Galvanized steel sheet thickness	1 mm
thickness of PCM basin (t_{PCM})	3 cm, 4 cm, 5 cm
Length of PCM basin (L_{PCM})	1.5 m
Width of PCM basin (w_{PCM})	1 m
Solar chimney angle	30°, 45°, 60°
Glass wool insulation thickness (t_{gw})	5 cm
Glass wool insulation thickness in the room floor	5 cm
Glass wool insulation thickness in the room roof	5 cm
Volume of the cooling room	1 m^3
Cooling room inlet diameter	7.62 cm
Dimension of the inlet opening at the room wall	0.2 m × 0.2 m
Dimension of the room outlet opening	0.15 m × 1 m
Wood thickness (w_d)	18 mm

Table 2
Physical and thermal properties of the materials.

Materials	Density (ρ) (kg/m^3)	Thermal conductivity (k) (W/m.K)	Specific heat capacity (C_P) (J/kg.K)
Air	1.225	0.0242	1005
Glass	2220	1.15	830
Glass wool	12	0.04	840
Aluminium sheet	2645	220.68	864.35
Galvanized steel	7767	197.65	815.53
Wood	721	0.159	1260

the PCM to the solar chimney, where three cases were made for different thicknesses of the storage tank of PCM (t_{PCM} = 3 cm, 4 cm, and 5 cm), and finally, the theoretical results were compared with the practical results. Fig. 1 shows the solar chimney with the room in 2-D and 3-D. A 3-D model was used to describe the solar chimney with room problem for natural ventilation. The room was made of wood, cubic size 1 m^3, connected at the top by a solar chimney at different tilt angles, and the room inlet was 0.04 m^2. All room models have the same dimensions of the solar chimney and absorber plate. A layer of wood sandwiched with a layer of glass wool (without PCM) are placed in both the roof and the floor of the room, and two layers of wood sandwiched with a layer of glass wool in the middle (with PCM) are placed behind the storage basin of PCM and both the roof and the floor of the room. Table 1 shows the dimensions of the models and materials specifications used in the theoretical analysis, and Table 2 shows the physical and thermal specifications of the materials used in the theoretical analysis. Their properties were examined in the laboratories of the College of Engineering, Department of Mechanics at the University of Basrah, and the Southern Technical University - Basrah Engineering Technical College.

2.1.2. *The governing equations*

2.1.2.1. Solar chimney without PCM. The air flow inside the solar chimney is produced by natural convection that results from renewable energy (solar radiation). The governing equations that used in the simulation contain of mass conservation for the Reynolds Averaged Navier Stokes equations, the energy, turbulence and radiation transfer equations. The governing equations (continuity, momentum, and energy) in the system were solved by using several assumptions to solve the present air flow and heat transfer. The assumptions for the solar chimney with or without PCM are outlined as follows:

1. Unsteady state conditions.
2. Density in buoyancy force is modeled by Boussinesq approximation is utilized.
3. Three-dimensional model.
4. Turbulent flow.
5. The flow is incompressible.
6. The PCM is incompressible.
7. Insulated walls of room is exposed to the solar radiation, and the room is subjected to different thermal boundary conditions along the test day: $\left(\frac{\partial T}{\partial x} \neq 0,\ \frac{\partial T}{\partial y} \neq 0\right)$.
8. No-slip conditions between the fluid and wall.
9. All the air properties are constant and they are evaluated at ambient temperature T_a = 309 K and the temperature inlet T_{in} = 300 K.
10. The solar chimney with the room located facing south at 30.568738° latitude and 47.749277° longitude has been studied in both theoretical and experimental work.
11. Viscous dissipation and compression work are assumed negligibly small.

The governing equations include a set of Kronecker delta symbols δijδij for the continuity, momentum, and energy equations, as shown below [4]:

- Continuity equation:

$$\frac{\partial \rho}{\partial t} + \frac{\partial u_i}{\partial x_i} = 0 \tag{1}$$

- Momentum equation

$$\rho\frac{Du_i}{Dt} = -\frac{\partial P}{\partial x_i} + \frac{\partial}{\partial x_j}\left[\mu\left(\frac{\partial u_i}{\partial x_j} + \frac{\partial u_j}{\partial x_i}\right) - \rho\overline{u_l' u_J'}\right] + \rho g_i \beta (T - T_a) \tag{2}$$

- Energy equation

$$\rho C_P \frac{DT}{Dt} = \frac{\partial}{\partial x_j}\left[k\frac{\partial T}{\partial x_j} - \rho C_P \overline{u_J' T'}\right] \tag{3}$$

$$\frac{DT}{Dt} = \frac{\partial}{\partial x_j}\left[\frac{k}{\rho C_P}\frac{\partial T}{\partial x_j} - \overline{u_J' T'}\right] \tag{4}$$

$$\alpha = \frac{k}{\rho C_P} \tag{5}$$

$$\frac{DT}{Dt} = \frac{\partial}{\partial x_j}\left[\alpha\frac{\partial T}{\partial x_j} - \overline{u_J' T'}\right] \tag{6}$$

$$\frac{D}{Dt} = \frac{\partial}{\partial t} + u\frac{\partial}{\partial x} + v\frac{\partial}{\partial y} + w\frac{\partial}{\partial z} \tag{7}$$

$$\frac{DT}{Dt} = \frac{\partial T}{\partial t} + u\frac{\partial T}{\partial x} + v\frac{\partial T}{\partial y} + w\frac{\partial T}{\partial z} \tag{8}$$

$x_j = x$, y, z and $u_j = u$, v, w

The finial energy equation becomes:

$$\frac{\partial T}{\partial t} + u\frac{\partial T}{\partial x} + v\frac{\partial T}{\partial y} + w\frac{\partial T}{\partial z} = \frac{\partial}{\partial x}\left(\alpha\frac{\partial T}{\partial x}\right) + \frac{\partial}{\partial y}\left(\alpha\frac{\partial T}{\partial y}\right) + \frac{\partial}{\partial z}\left(\alpha\frac{\partial T}{\partial z}\right) \tag{9}$$

Eq. (7) called material derivative [17], $\rho g\beta(T - T_a)$: is the buoyancy source, α: thermal diffusivity, u_i: velocity components in the directions X_i, X_j. *T, P* temperature and pressure respectively. μ is viscosity, $\overline{u_J' T'}$ the turbulent heat transfer is evaluated by an opposite turbulence model, $\rho\overline{u_l' u_J'}$ is the turbulent Reynold's stress. By adopting the turbulent viscosity models are calculated as [18]:

Turbulent Reynolds stresses:

$$-\rho\overline{u_l' u_J'} = \mu_t\left(\frac{\partial u_i}{\partial x_j} + \frac{\partial u_j}{\partial x_i}\right) - \frac{2}{3}\rho k\delta_{ij} \tag{10}$$

Turbulent heat transfer:

$$-\rho\overline{u_J' T'} = \frac{\mu_t}{Pr_i}\frac{\partial T}{\partial x_j} \tag{11}$$

Where: μ_t is the turbulent dynamic viscosity, Pr_i the Prandtl number. δij Kronecker delta, $\delta ij = 1$ if $i = j$ and $\delta ij = 0$ if $i \neq j$. The surface azimuth angle equal zero for south direction.

2.1.2.2. Solar chimney with PCM

The mathematical simulations in solving the problem include unsteady equations of continuity, momentum, and energy equations, the conservation of mass and momentum equations for air are the same as for PCM, as follows [4,19,20]:

- Continuity equation

$$\frac{\partial \rho_{PCM}}{\partial t} + \frac{\partial u_i}{\partial x_i} = 0 \tag{12}$$

- Momentum equation

$$\rho_{PCM}\frac{Du_i}{Dt} = -\frac{\partial P}{\partial x_i} + \frac{\partial}{\partial x_j}\left[\mu_{PCM}\left(\frac{\partial u_i}{\partial x_j} + \frac{\partial u_j}{\partial x_i}\right)\right] + \frac{(1-\gamma)^2}{(\gamma^3 + \Gamma)^3}A_{mush}u_i + \rho_{PCM}g_i\beta_{PCM}(T - T_a) \tag{13}$$

- Energy equation

For PCM-zone:

$$(\rho Cp)_{PCM}\frac{DT}{Dt} = \frac{\partial}{\partial x_j}\left[k_{PCM}\frac{\partial T}{\partial x_j}\right] - \rho_{PCM}H_L\frac{\partial \gamma}{\partial T} \tag{14}$$

$$H_L = h_{ref} + \int_{T_{ref}}^{T} C\,dT + \gamma L \tag{15}$$

Where: H_L is the enthalpy of the PCM, h_{ref}: is the reference enthalpy, T_{ref}: is the reference temperature, *C*: as the specific heat capacity of the PCM in the corresponding phase (e.g., solid, liquid, or mixed) [21], *L*: is the latent heat.

For Aluminium:

$$\frac{\partial^2 solid}{\partial x^2} + \frac{\partial^2 T_{solid}}{\partial y^2} + \frac{\partial^2 T_{solid}}{\partial z^2} = \frac{1}{\alpha_{solid}}\frac{\partial T_{solid}}{\partial t} \tag{16}$$

Where: t is the time, ρ_{PCM} is the density of PCM, β_{PCM}: is the thermal expansion coefficient of PCM, μ_{PCM} is the viscosity of the PCM, *P* is the pressure, γ is the liquid fraction, Γ is a small number less than 0.001 to prevent division by zero [4,22]. A_{mush} is the mushy zone constant that acts as a velocity damping factor to zero during the solidification process. The value of the mushy zone constant ranges from 10^4 to 10^7, but [23], found that 10^5 gives the best results when performs simulations for a range of its values. The g_i is the gravitational acceleration, where its value in the x and z-direction is (0 m/s^2), while in the y-direction it is equal to (-9.81 m/s^2). The γ is a liquid fraction, which is calculated in each iteration and depending on the enthalpy balance, the liquid fraction region is determined between 0 and 1 and is known as the mushy zone [24].

The mushy zone region is the rage of temperature between $T_{liquidus}$ and $T_{soildus}$. $T_{liquidus}$ is the temperature which the PCM is fully liquid and $T_{soildus}$ is the temperature below which the PCM is fully solid. The value of liquid fraction (γ) during the phase change between the liquid and solid state when the temperature is $T_l > T > T_s$ is then [25]:

$$\gamma = \begin{pmatrix} 0\ for\ T < T_{soildus} \\ \dfrac{T - T_{solidus}}{T_{liquidus} - T_{solidus}}\ for\ T_{liquidus} < T < T_{solidus} \\ 1\ for\ T > T_{liquidus} \end{pmatrix} \tag{17}$$

Where: *T* is the local temperature. Accordingly, the velocity is affected as following:

$V = V_1$ in the liquid phase

$V = \gamma V_1$ in the mushy zone

$V = 0$ in the solid phase (18)

Where: *V* superficial velocity (average velocity) and V_1 the actual fluid velocity [24].

2.1.2.3. Turbulence model. To express the turbulent in solar radiation or heat fluxes and turbulent viscosity stresses, many turbulence models can be used to concept the turbulent viscosity or turbulent diffusion. The RNG k- epsilon model is based on the renormalization collection analysis of the Navier–Stokes equations suggested by [26]. This model contains

Table 3
Constants for the RNG (k – ε) model [29].

$C_{\varepsilon 2RNG}$	β_{RNG}	$C_{\mu RNG}$	$\sigma_{\varepsilon RNG}$	σ_{kRNG}	$C\mu$
1.68	0.012	0.0845	0.7179	0.7179	0.09

an expression in the equation of turbulent energy dissipation rate, and the effect of vortex flow. Consequently, it gives a good accuracy for swirl flows. The equations for kinetic turbulence and dissipation are the same as for the standard k-ε model, but the model constants are different and the constant $C_{\varepsilon 1}$ is replaced by $C_{\varepsilon 1RNG}$. The transport equation for turbulence dissipation becomes is as follows [27,28]:

1. Turbulence kinetic energy (k):

$$\frac{\partial}{\partial t}(\rho k)+\frac{\partial}{\partial x_i}(\rho k u_i)=\frac{\partial}{\partial x_i}\left(\frac{\mu}{\sigma_{kRNG}}\frac{\partial k}{\partial x_i}\right)+\mu_t\left(\frac{\partial u_i}{\partial x_j}+\frac{\partial u_j}{\partial u_i}\right)\frac{\partial u_i}{\partial x_j}-\rho\varepsilon \tag{19}$$

2. Dissipation rate (ε)

$$\frac{\partial}{\partial t}(\rho\varepsilon)+\frac{\partial}{\partial x_i}(\rho\varepsilon u_i)=\frac{\partial}{\partial x_j}\left[\left(\mu+\frac{\mu_t}{\sigma_{\varepsilon RNG}}\right)\frac{\partial\varepsilon}{\partial x_j}\right]\frac{\varepsilon}{k}\left(C_{\varepsilon 1RNG}\,G+C_{\varepsilon 2RNG}\,\rho\varepsilon\right) \tag{20}$$

$$\mu_t=\frac{C_\mu\rho k^2}{\varepsilon} \tag{21}$$

$$C_{\varepsilon 1RNG}=1.42-f_\eta \tag{22}$$

$$f\eta=\frac{\eta\left(1-\frac{\eta}{4.38}\right)}{(1+\beta_{RNG}\eta^3)} \tag{23}$$

$$\eta=\sqrt{\frac{G}{\rho C_{\mu RNG}\varepsilon}} \tag{24}$$

$$G=\mu_t\left[2\left(\left(\frac{\partial u}{\partial x}\right)^2+\left(\frac{\partial v}{\partial y}\right)^2+\left(\frac{\partial w}{\partial z}\right)^2\right)+\left(\frac{\partial u}{\partial y}+\frac{\partial v}{\partial x}\right)^2+\left(\frac{\partial u}{\partial z}+\frac{\partial w}{\partial x}\right)^2+\left(\frac{\partial v}{\partial z}+\frac{\partial w}{\partial y}\right)^2\right] \tag{25}$$

$$G=\mu_t\left(\frac{\partial u_i}{\partial x_j}+\frac{\partial u_j}{\partial u_i}\right)\frac{\partial u_i}{\partial x_j} \tag{26}$$

Where: k: turbulence kinetic energy, μ is viscosity, μ_t is the turbulent viscosity, $f\eta$, η turbulent model coefficient, G: is the generation of turbulent kinetic energy due to the mean velocity gradient or shear. This model considers one of usable model in low stratified tank [29]. The constants of the turbulence model are given in Table 3.

2.1.3. Initial and boundary conditions

For any appropriate try to solve any problematic there must be application of boundary conditions. The initial condition for the temperature of the solar chimney with the room was 300 K at inlet room and 309 K for the ambient temperature. The boundary conditions for the geometrical symmetric shape as it is shown in Fig. 2, and based on the previous assumptions, the boundary and initial condition for the solar chimney with room:

Initial conditions:

- Temperature: all external walls with ambient conditions $T = T_a =$ 309 K and the temperature at inlet room $T_{in} = 300$ K for all cases, except the comparison between theoretical and experimental work.
- Velocity: as pressure inlet $P_{in} = 0$.
- The kinetic energy and dissipation rate at the inlet can be roughly approximated for internal flow using the turbulence intensity T*i* and the characteristic duct length L. This approximation is based on the following assumptions [17]:

$$k=\frac{2}{3}(u_{in}Ti)^2 \tag{27}$$

$$\varepsilon=C_\mu^{\frac{3}{4}}\frac{k^{\frac{3}{2}}}{l} \tag{28}$$

$$l=0.07\,L \tag{29}$$

Where: Ti: turbulence intensity (0.05), l: depth of chimney or room height, and u_{in}: reference mean flow velocity [30].

Boundary conditions:

- Outlet boundary condition: pressure outlet boundary at atmospheric pressure $P_{out} = 0$.
- The exterior boundaries at the top of the room and the back of the chimney are insulated:

$\frac{\partial T}{\partial n}=0$, where: $n = x$, y, and z direction.

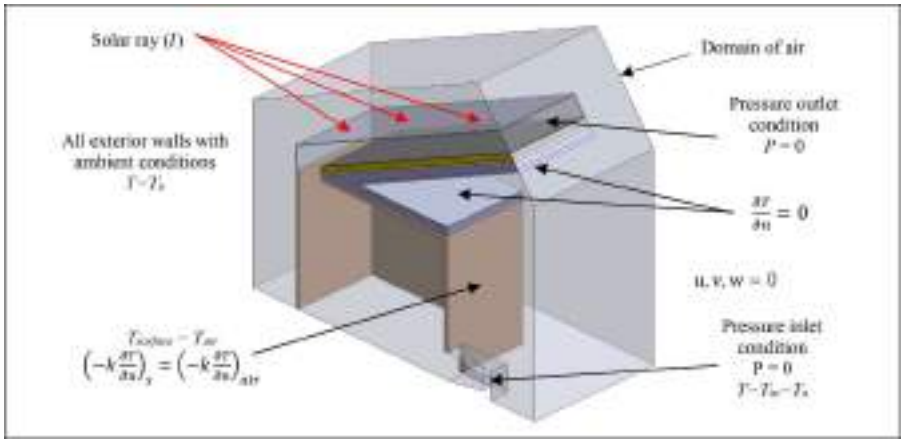

Fig. 2. Boundary types of domains for a solar chimney with a symmetric shape.

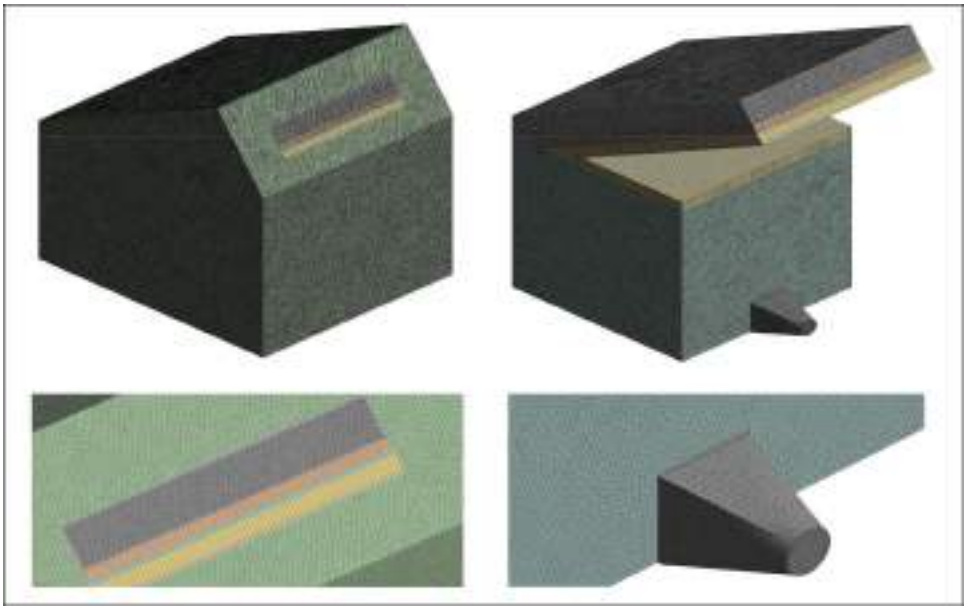

Fig. 3. The mesh generation for the model (solar chimney with room and PCM) with display the inlet and outlet openings.

Table 4
Grid independence test result for the solar chimney with the room and PCM.

Mesh	No. of element	ACH
Mesh – 1	995,423	43.802
Mesh – 2	1,526,534	44.108
Mesh – 3	1,804,112	45.665
Mesh – 4	2,685,126	46.6
Mesh – 5	3,812,617	46.7

- No slip walls u, v, $w = 0$.
- All the surfaces contact with air, and all interior walls with continuous boundary conditions are:

$$T_{savface} = T_{air} \rightarrow \left(-k\frac{\partial T}{\partial n}\right)_{surface} = \left(-k\frac{\partial T}{\partial n}\right)_{air}$$

- The device was subjected to solar ray (I) and its variation with time, and the intensity of solar radiation.
- The kinetic energy of turbulent and the rate of dissipation at the leaving:

$$\left.\frac{\partial k}{\partial x}\right|_{y=L} = \left.\frac{\partial \varepsilon}{\partial x}\right|_{y=L} = 0$$

- The area surrounding the device has an ambient air temperature $T = T_a$.

2.1.4. Mesh generation and independency test

The initial stage of the finite volume approach involves the creation of the grid. Grid generation involves partitioning the working area into smaller parts. The process of meshing directly affects the accuracy and convergence of computational fluid dynamics (CFD) [31]. The generated model was fragmented into smaller components using basic form elements that were linked at shared nodes. The hexahedron and tetrahedron were chosen for this study because of their complex geometry. Fig. 3 for the solar chimney with room and PCM displays different sorts of 3-D mesh elements used in ANSYS-Fluent 2021/R2.

To ensure that the results are influenced only by the boundary conditions and physics employed, rather than the mesh resolution, it is essential to perform a mesh independence study. A commonly used approach to assessing grid independence involves systematically increasing the resolution and conducting repeated simulations. Calculations have been performed for five specific grid sizes. The findings of the grid independence test for the room with a solar chimney and PCM are summarized in Table 4.

It was noted that the numbers of elements 2,685,126 and 3,812,617 were nearly identical. Therefore, a domain consisting of 2,685,126

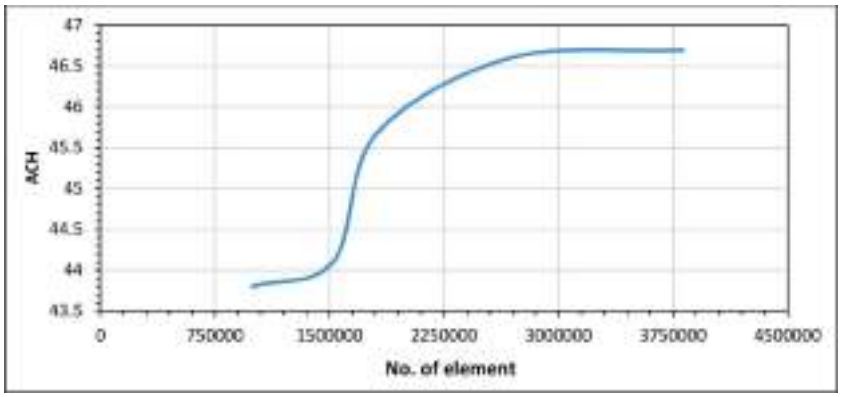

Fig. 4. Variation of air change per hour (ACH) with total element number for solar chimney with room and PCM.

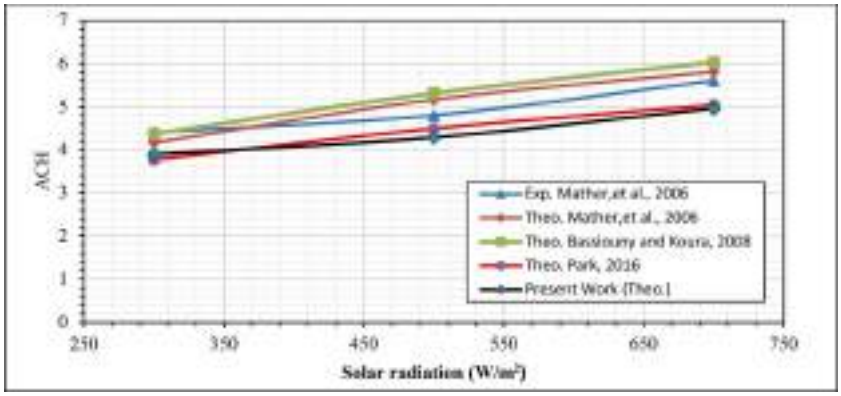

Fig. 5. Variation of solar radiation with ACH, solar radiation angel $\beta = 55^{\circ}$, comparing with simulations and experiments for previous studies.

Table 5
Summary of ACH for present work comparing with simulations and experiments for previous studies.

Air gap (m)	Chimney inlet (height) (m)	I (W/m^2)	ACH					Error % with [34]
			Exp [33]	Theo [33]	Theo. [32]	Theo. [34]	Theo. Present work	
0.3	0.3	300	4.4	4.17	4.37	3.77	3.89418	3.2938
		500	4.8	5.16	5.31	4.49	4.286604	4.5299
		700	5.6	5.81	6.03	5.04	4.95648	1.6571

Fig. 6. Photo of the solar chimney with room experimental system.

elements was selected in order to enhance computational accuracy and minimize calculation time. Fig. 4 displays the variation of ACH with the number of elements for a solar chimney with PCM.

2.1.5. Validation

In order to verify the validity of the simulation for the numerical model of the solar chimney with room in the soft package ANSES-Fluent/2021/R2, a comparison was made with the results of several numerical and experimental studies conducted by [32–34] as shown in Fig. 5 and Table 5. The results showed good agreement between the numerical results and the results of the other researchers. When calculating the ACH, there is an acceptable error, as the error rate reached 3.16 %, and this value falls within the acceptable error range and is considered a relatively low value.

2.2. Experiment setup

2.2.1. Components of experimental design

The specifications and the most important practical steps that will be performed on an experimental model of a solar chimney towards the south with the presence of phase change material. This includes working on studying the behavior of the solar collector in the presence and absence of a phase change material. This build model for experimental work is located in the College of Engineering at the University of Basrah in the city of Basrah-Iraq, which is located at 47.749277° longitude and 30.568738° latitude, with the solar chimney facing south. The system consists of the following parts: Solar chimney (aluminum plate, PCM basin, galvanized steel container for phase change material, transparent cover), small size cooling room, and measuring device as shown in Fig. 6.

Fig. 7. Construction of ventilation room model.

Fig. 8. Stages of manufacturing the inclined solar chimney.

2.2.2. Ventilation room design

The room was built of wood with a thickness of 18 mm, except for the ceiling and floor of the room, it consists of three layers, two layers of wood 18 mm thick, with a layer of glass wool (insulation) 5 cm thick in the middle. The room is cubic with a size of 1 m^3. The room includes an inlet and outlet opening, the inlet opening located in the middle of the lower part of the north wall, opposite the outlet opening located at the top of the ceiling of the room, a solar chimney connected to the room

Fig. 9. Photograph of PCM placed in a basin for a solar chimney.

Table 6
Phase change material (PCM) properties.

Parameters	Symbol	Value	Unit
Density	ρ	894	kg/m^3
Thermal conductivity	K	0.2	W/m. K
Specific heat capacity (solid phase)	c_{PS}	2.9	kJ/kg. K
Specific heat capacity (liquid phase)	c_{PL}	2.2	kJ/kg. K
Melting point	tm	340	K
Dynamic viscosity	μ	0.006	kg/m. s
Kinematic viscosity	ν	6.713	mm^2/s
Melting heat	h_m	70.006	kJ/kg
Thermal expansion	β	0.125	——
Solidus temperature	T_{Sus}	292	K
Liquidus temperature	T_{Lus}	300	K

from the outlet. A small, tightly sealed door measuring (60 × 70) cm is installed to prevent air from entering or leaving the room. The purpose of this design is to calculate and compare the air flow rate, the efficiency of PCM in storage and excreting heat at night, and the flow patterns. Fig. 7 shows the stages of ventilation room construction.

2.2.3. Solar chimney design

The solar chimney is one of the most important parts of the system. The solar radiation is transmitted to the aluminum plate connected to the PCM basin. The chimney is designed as a rectangular box with a length of 1.5 m, a width of 1 m for the PCM basin, and a gap of 0.15 m for the glass. The solar chimney channel consists of two sides, one of which is transparent glass with a thickness of 4 mm, and the other face is the absorbent surface made of aluminum sheets with a thickness of 1 mm and the PCM container behind the aluminum sheets. The model insulates the PCM container with three layers: a first layer of 18 mm thick wood, a second layer of 5 cm thick glass wool, and a third layer of 18 mm thick wood. The area of the solar chimney roof (glass) is 1.5 m^2, and the total area of the solar collector (glass) is 2.1 m^2. The thickness of the PCM basin is 4 cm. The aluminum layer placed on the PCM container under the roof of the chimney is coated with black paint to increase the heat absorber. The solar chimney faces south and tilts at a 30° angle. Fig. 8 explains the steps of solar chimney construction.

2.2.4. Phase change material (PCM) (Paraffin wax)

Phase change materials for momentary heat storage to balance temperature changes and energy storage are used in many practical applications in the electronics and automotive industry as well as in buildings. Phase change material storage is preferred over reasonable heat storage in applications with little temperature fluctuation due to its semi-thermal storage mechanism and high storage density. The container contains 75 kg of the PCM used in the present work, which is paraffin wax as shown in Fig. 9, where a PCM is placed in the basin after melting it through normal heating. The specifications were examined at the University of Basrah - College of Science, Shuaiba refinery in Basarh and the Ministry of Science and Technology in Iraq, as shown in Table 6. The PCM was placed inside a container made of galvanized iron, thus storing and releasing the excess heat energy from solar radiation at

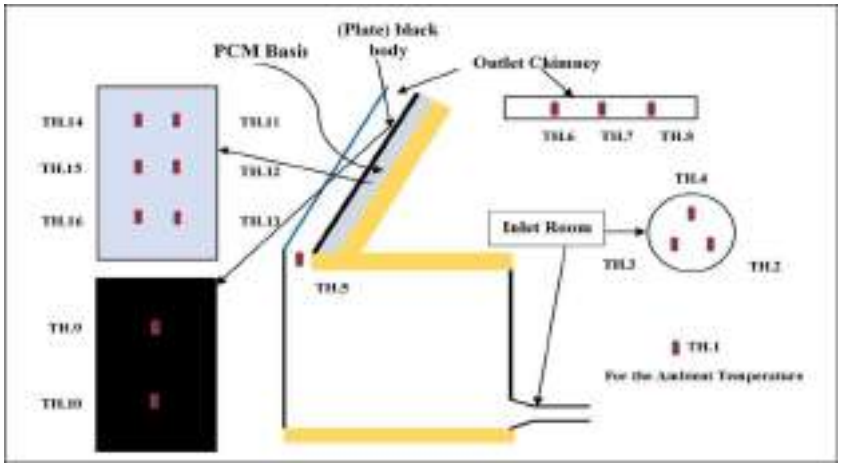

Fig. 10. Locations and numbers of thermocouples with enlarged parts.

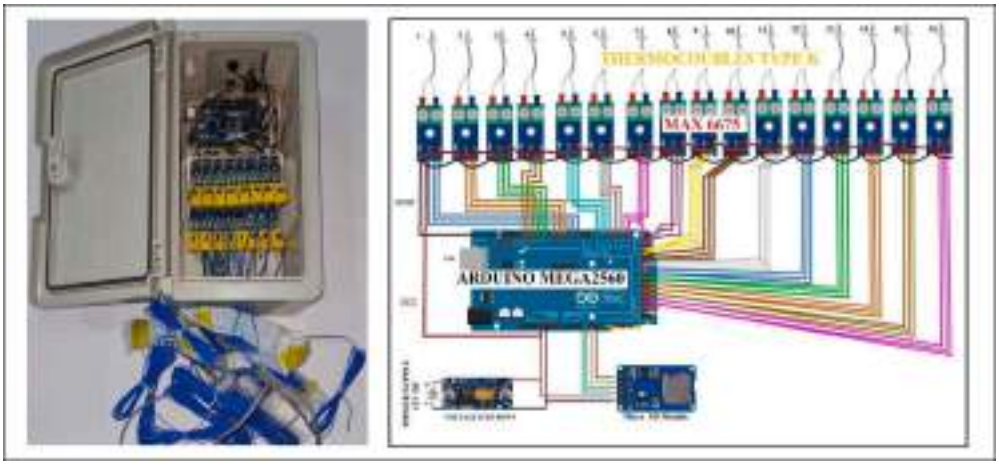

Fig. 11. Data logger device and connected parts.

Fig. 12. Hot wire anemometer (GM8903).

Table 7
Hot wire anemometer (GM8903) specifications.

Function	Measuring range	Resolution	Accuracy	Error
Air velocity	0 – 30 m/s	0.1 m/s	±3%	± 0.1 dgts

active time.

2.2.5. Measurement devices

2.2.5.1. Multi – channel data logger. In this study, 16 thermocouples were used. The K-type thermocouple sensor measures the temperature on the cable end, and the temperature is monitored in a powerful way. The connector is a standard small K-male with two flat pins, allowing good and easy communication with the transmitter. The thermocouples measure the temperature in any location and are widely available. They have multiple lengths as well as measuring the range of temperatures (-25 – 125) °C and the tolerance (± 1.5) °C. Fig. 10 shows the locations and numbers of thermocouples. All thermocouples were connected to a multi-channel Arduino (Mega 2560), which is programmed to measure and record temperatures with a 1 h. time step during the whole experimental period and contains an amplifier called MAX6675 (adapter) to amplify the signal coming from the thermocouple because it is very weak. The collected data is continuously stored in a memory card with a capacity of 32 GB that has been placed in storage that can be stored for 10 continuous days and then exported to a PC at the end of the experiment. Fig. 11 shows the data logger device and the parts connecting with each other to configure the device.

2.2.5.2. Hot wire anemometer (GM9803). The anemometer instrument type GM9803 is used to measure air velocity, temperature, and air quantity. It operates at temperatures ranging from -10 to 50 °C with a humidity of 40%–85% RH. The device can record 350 readings and store them. Fig. 12 illustrates the hot wire anemometer. The air velocity was measured at the inlet and outlet openings of the solar chimney. Table 7 shows the specifications of the air velocity.

Fig. 13. Solar power meter (SM206-SOLAR).

Table 8
Solar power meter (SM206-SOLAR) specifications.

Function	Measuring range	Resolution	Error
Solar radiation	0.1–1999.9 W/m^2	0.1 W/m^2	± 10%

2.2.5.3. Solar power meter (SM206-SOLAR). This device is an accurate instrument type (SM206) for measuring the intensity of solar radiation. The device operates at a temperature of (0 – 40) °C and a relative humidity of 80 % (RH). Fig. 13 shows the solar power meter. During the experiment, the measurement was taken every hour during the daytime, where it was placed at the same angle as the solar chimney, and the direction of the sensor is in the direction of the incident radiation. Table 8 shows the specifications of the solar power meter.

2.2.6. Test procedure

The data collection period was in the following days (28, 29, 30/9/2023) in September and in October (14, 15, 16/10/2023), and the best readings were on 30/9/2023 and 15/10/2023 between 08:00 a.m. and 02:00 a.m. The solar chimney was placed facing south at an angle of 30°, the thickness of the air gap was 15 cm, and the thickness of the PCM basin was 4 cm. The tests were done at the University of Basrah, College of Engineering, at a rate of one day every hour. Data are taken for the average temperature of the surroundings, the PCM, absorber plate, inlet room, outlet solar chimney, and on its wall using thermocouples, as well as measuring the air velocity of the of the outlet solar chimney using a hot wire anemometer and measuring solar radiation using a solar power meter. The obtained data is then converted into a chart.

2.2.7. Methods of calculation

The method for calculating the average temperature of the PCM, absorber plate, room inlet, outlet solar collector and calculating the ventilation rate as follows:

2.2.7.1. Calculate ventilation rate (ACH). The average air velocity was read at the inlet of the heat exchanger and at the air outlet of the solar chimney, as in the following equation:

$$ACH = \frac{3600 \times Q_{vent.}}{V_r} \tag{30}$$

$$Q_{vent} = V_{av} \times V_{en} \tag{31}$$

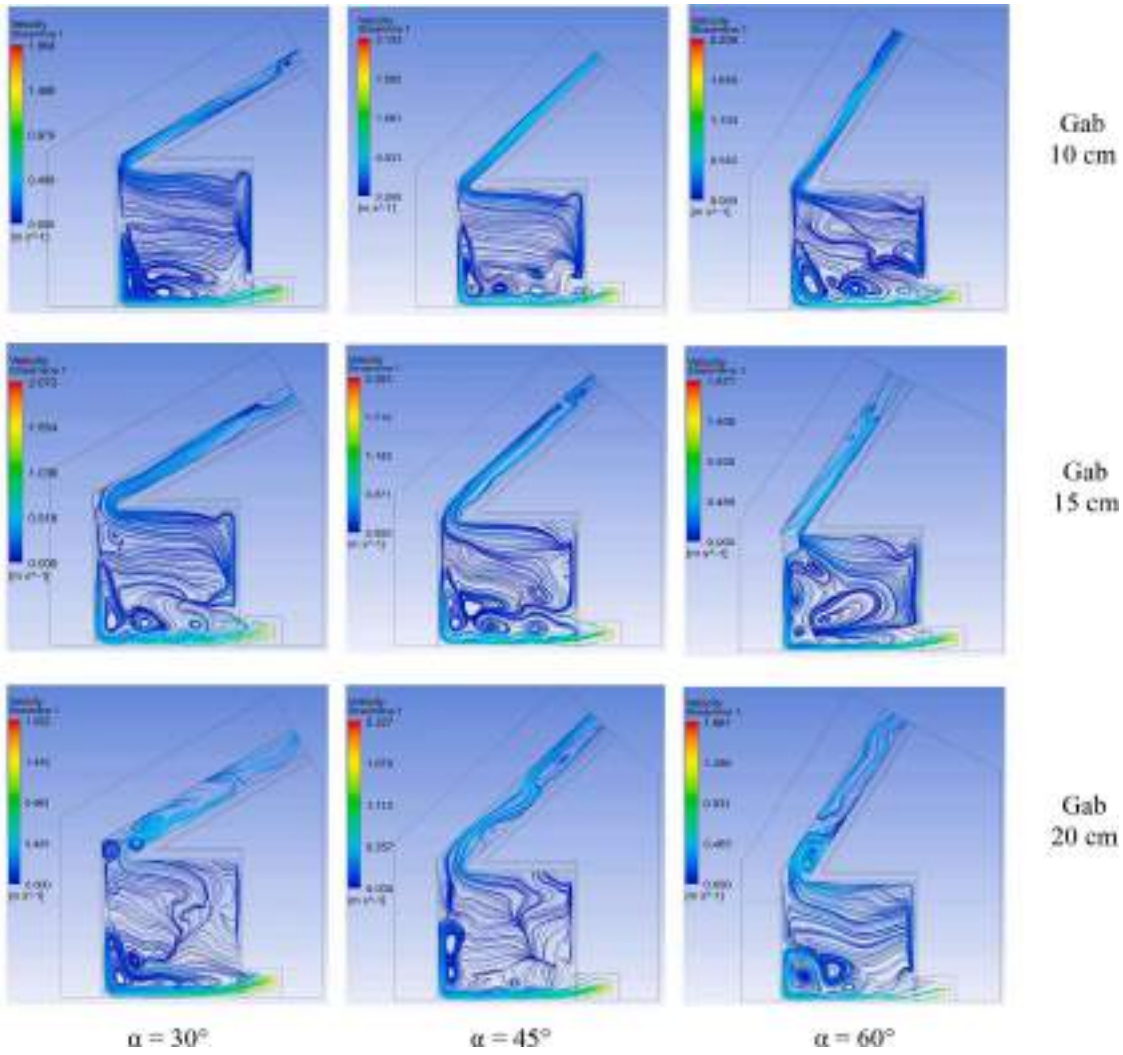

Fig. 14. Contours illustrate the streamlines for the room and solar chimney at 12 p. m., for different tilt angle of solar collector and different gab.

Where: V_r: room volume taken (1 × 1 × 1) m, $V_{av.}$: average velocity at the exit cross section of the chimney, $A_{en.}$: inlet cross section area of the chimney.

2.2.7.2. Calculate average temperature. Temperature sensors were distributed in the storage tank for the PCM (TH.11, TH.12, TH.13, TH.14, TH.15, TH.16), while sensors for measuring the temperature of the absorber plate (TH.9, TH.10), the average outlet temperature from the solar chimney (TH.6, TH.7, TH.8) and the average temperature for the inlet room (TH.2, TH.3, TH4) are calculated in every hour as follows:

$$T_{PCM.av} = \frac{TH.11 + TH.12 + TH.13 + TH.14 + TH.15 + TH.16}{6} \quad \text{for PCM} \tag{32}$$

$$T_{ab.av} = \frac{TH.9 + TH.10}{2} \quad \text{for absorber plate} \tag{33}$$

$$T_{outlet\ S.Ch.av} = \frac{TH.6 + TH.7 + TH.8}{3} \quad \text{for outlet solar chimney} \tag{34}$$

$$T_{outlet\ H.E} = \frac{TH.2 + TH.3 + TH.4}{3} \quad \text{for inlet room} \tag{35}$$

3. Results and discussion

3.1. Numerical results

Fig. 14 shows the contours of streamlines for the solar chimney and room, the numerical study was performed at 12 p. m., different gab of solar chimney (gab = 10 cm, 15 cm, and 20 cm) and with different tilt angle (α = 30°, 45°, and 60°). It can be seen that the streamlines are distributed toward the inlet opening of the solar chimney. We can notice from the figure that at angle 30° and the air gap 15 cm, the streamlines are almost not straight. At angle 45° and the air gap 10 cm, the streamlines are straight and directed towards the outside of the solar chimney. For angle 60°, there is resistance to air escaping and the formation of vortexes in the solar chimney and its ends that prevent or cause resistance to air escaping. There is also the presence of eddies inside the room, and this indicates the presence of the driven bouncy force to flow inside the room. We notice at angle 30° and air gap 15 cm, the stream lines are almost irregular, which means that the flow is turbulent, which indicates are gives the best ventilation.

Fig. 15 shows the contours of temperature for the solar chimney and room, the numerical study was performed at 12 p. m., different gab of solar chimney (gab = 10 cm, 15 cm, and 20 cm) and with different tilt angle (α = 30°, 45°, and 60°). It can be noted that the at α = 30° and gab = 15 cm, the temperature of plate collector was maximum (360.919 K) at noon 12 p.m., because the solar radiation falling on the solar collector

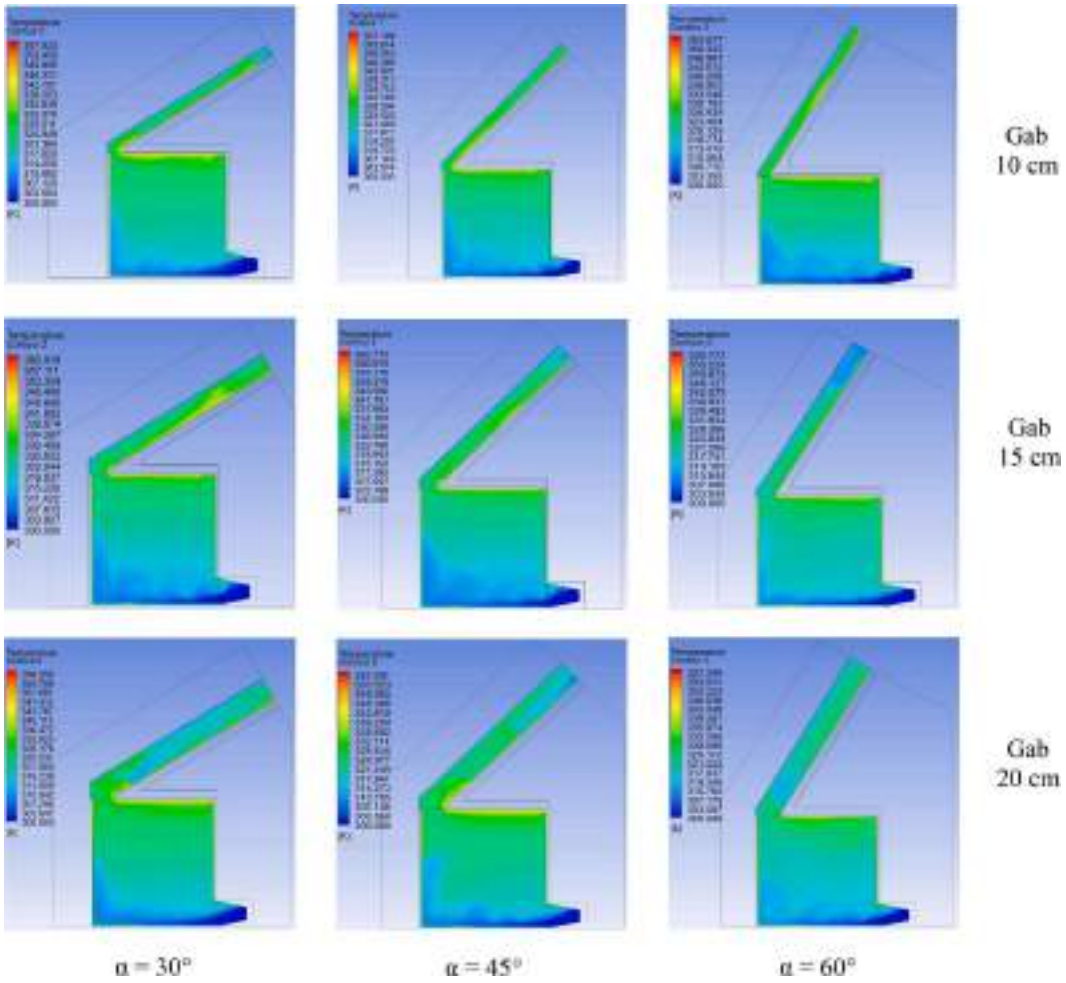

Fig. 15. Contours illustrate the temperature for the room and solar chimney at 12 p. m., for different tilt angle of solar collector and different gab.

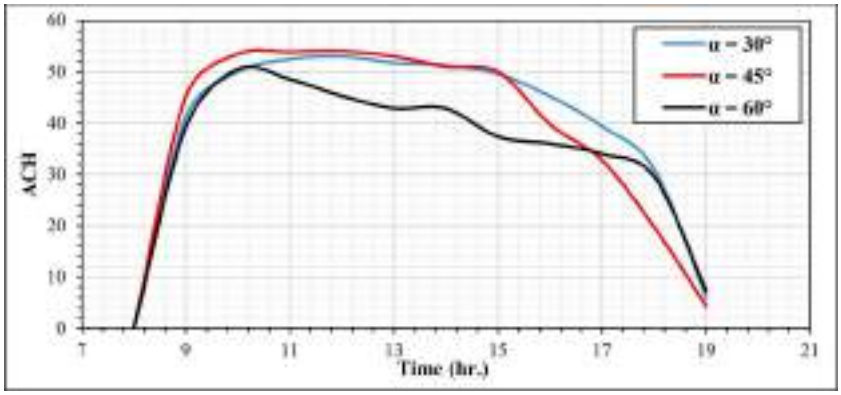

Fig. 16. Air change per hour (ACH) with time at gab = 15 cm and different tilt angle of the solar chimney (α = 30°, 45°, 60°).

at an angle of 30 is more vertical than at other angles, and therefore the amount of heat is greater, which present the driven bouncy force to air flow inside the room, leading to more natural ventilation by outlet opening for solar chimney. Also, the high temperature at the surface of heat absorbing plate for collector and extended to the celling of room. This temperature increases on the surface as solar radiation decreases over time, and this temperature is due to the decrease in the ventilation rate resulting from the decrease in solar radiation. High solar flux intensity also raises the temperature of the wood, impacting the heat transfer to the room.

Fig. 16 illustrates the variation of the inclined angle (α = 30°, 45°, and 60°) on the Air Changes per Hour (ACH) over time, with a gap of 15 cm. It can be seen from this figure that at an angle of 30°, the amount of ACH is greater throughout the day. However, at an angle of 45°, the ACH reaches a maximum value of 54.0275 1/h at 12 p.m., while at an angle of 60°, the ACH is the lowest from these angles. When calculating the ACH every hour from 8 a.m. to 7 p.m., it was found that the total of ACH at angle 30° is 481.296 1/h, at angle 45° is 467.7922 1/h, and at angle 60° is 424.3514 1/h, as shown in Table 9, this indicates that when decrease the inclination angle, increase the rate of air change during the day,

Table 9
Solar radiation at absorber plate and ACH with different tilt angle and time.

Time (hr.)	α = 30°		α = 45°		α = 60°	
	Solar radiation at absorber plate (W/m^2)	ACH	Solar radiation at absorber plate (W/m^2)	ACH	Solar radiation at absorber plate (W/m^2)	ACH
8 a.m.	145.254	10.2225	155.624	10.4258	160.245	10.6241
9 a.m.	459.381	41.2546	411.977	45.2608	306.172	39.2759
10 a.m.	563.147	49.9657	545.623	53.4994	510.642	50.5586
11 a.m.	605.128	52.4845	560.145	53.9	489.325	48.5517
12 p.m.	630.775	53	584.572	54.0274	463.79	45.2999
1 p.m.	590.544	51.7706	555.687	53	415.856	42.9241
2 p.m.	590.143	51.3045	480.741	51.0352	391.654	42.8455
3 p.m.	311.335	49.5533	364.364	50	251.98	37.3831
4 p.m.	240.652	45.2586	269.254	39.7972	243.846	36
5 p.m.	160.245	39.3809	187.576	32.7237	202.254	34
6 p.m.	51.0916	31.0715	18.2	19.7615	18.4996	29.6009
7 p.m.	10.245	6.0293	8.124	4.3612	14.5874	7.2876
Total ACH		481.296		467.7922		424.3514

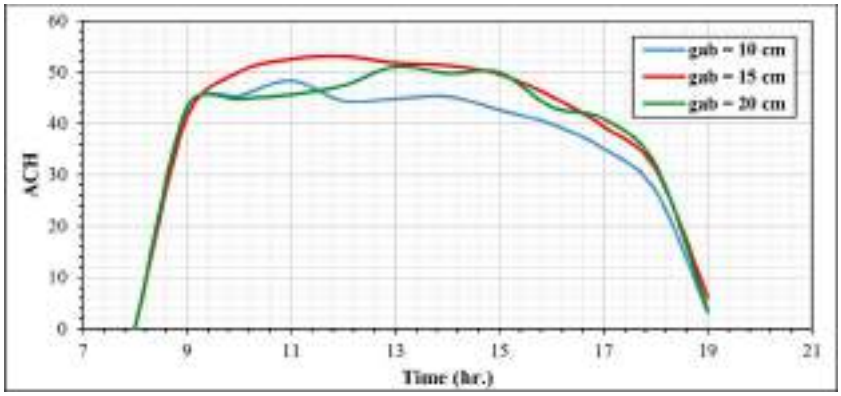

Fig. 17. Air change per hour (ACH) with time at tilt angle of the solar collector α = 30° and different gab = 10 cm, 15 cm and 20 cm.

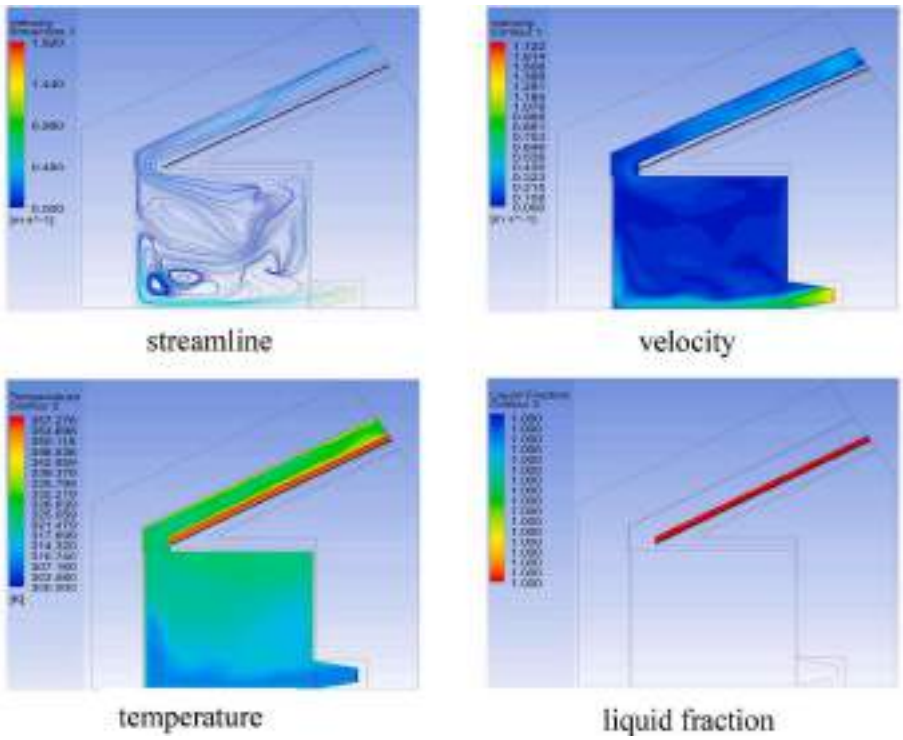

Fig. 18. Contours illustrate the effect of streamline, velocity, temperature distribution, and liquid fraction in the room and solar chimney with PCM at gab = 15 cm, α = 30°, 3 p.m., for basin thickness (t_{PCM} = 3 cm).

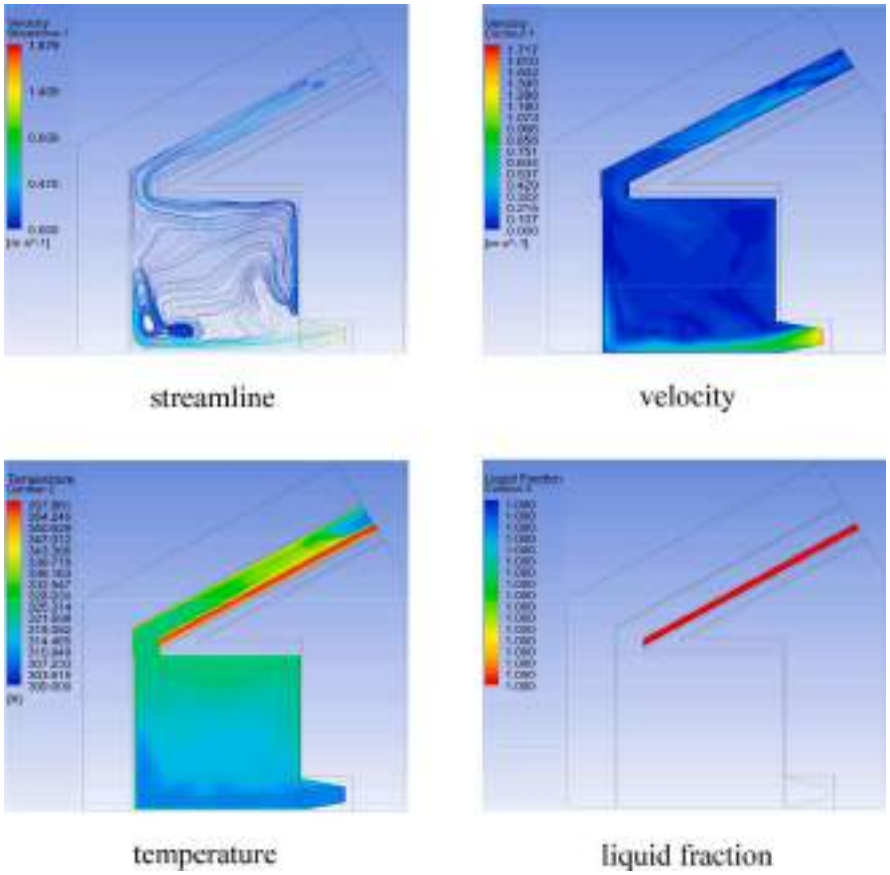

Fig. 19. Contours illustrate the effect of streamline, velocity, temperature distribution, and liquid fraction in the room and solar chimney with PCM at gab = 15 cm, α = 30°, 3 p.m., for basin thickness (t_{PCM} = 4 cm).

where the angle 30° heats the air more effectively, resulting to a greater temperature difference. This difference creates stronger buoyancy forces, which increases air flow and improving the ventilation rate, this means the heat gain during the day for angle 30° is greater than the other angles. After noon the ACH decrease due to decrease the solar radiation for all cases. Also note from Table 9, that from 9 a.m. to 2 p.m. the intensity of solar radiation at angle 30° is greater than at angle 45° and the convection currents or buoyancy force at angle 30° is more inclined with the direction of flow, which causes flow obstruction and decreases ACH. For the period from 4 p.m. to 6 p.m., due to the change in the direction of incident solar radiation, the intensity of radiation at angle 45° is greater than at angle 30°, which makes the convection currents on flow obstruction weak, which leads to an increase in velocity and thus an increase in ACH.

Fig. 17 illustrates the effect of ACH over time at a tilt angle of solar chimney α = 30° for different air gaps in the solar collector (gab = 10 cm, 15 cm, and 20 cm). The figure shows that the highest ACH occurs with a 15 cm gap, due to the increased temperature of the solar chimney resulting from greater solar radiation, the amount of air at gab = 15 cm is suitable for the heat exchange process between the absorber plate and the air. Additionally, it is evident that the lowest ACH is observed with a 10 cm air gap in the solar chimney.

Fig. 18 shows the contours of streamlines, velocity, temperature, and liquid fraction for solar chimney with room at basin thickness of PCM (t_{PCM}) = 3 cm. The air gab is 15 cm and α = 30° where the time 3 p. m. It can be noted that the maximum velocity and streamline at the inlet where the minimum cross section area, where the maximum velocity is 1.722 m/s. As for the flow streamlines inside the ventilation room, eddies form in the lower left corner of the room. Also, the temperature of the absorber plate is maximum and reach to 357.278 K, While the ambient temperature is 309 K, the temperature difference is due to the installation of the solar chimney designed for the purpose of air circulation. The time of convert the PCM from solid to liquid is enough where the melting fraction (liquid fraction) is equal to 1.

Fig. 19 shows the contours of streamlines, velocity, temperature, and liquid fraction for solar chimney with room at basin thickness of PCM (t_{PCM}) = 4 cm. The air gab is 15 cm and α = 30° where the time 3 p. m. It can be seen that the maximum velocity and streamline at the inlet where the minimum cross section area, where the maximum velocity is 1.717 m/s, this velocity plays an important role in transferring heat from the room to the outside, but the streamlines are almost irregular and form more vortexes than in the case when the thickness of the PCM basin is 3 cm, this indicates an increase in the rate of air change per hour. As for the flow streamlines inside the ventilation room, eddies form in the lower left corner of the room, the design of the solar chimney causes natural free convection inside the room. Also, the temperature of absorber plate is maximum and reach to 357.861 K. The time of convert the PCM from solid to liquid is enough where the melting fraction (liquid fraction) is equal to 1, this means that the PCM are melted and are in the liquid state.

Fig. 20 shows the contours of streamlines, velocity, temperature, and liquid fraction for solar chimney with room at basin thickness of PCM (t_{PCM}) = 5 cm. The air gab is 15 cm and α = 30° where the time 3 p. m. This figure show that the maximum velocity and streamline at the inlet where the minimum cross section area, where the maximum velocity is 1.424 m/s. As for the flow streamlines inside the ventilation room, eddies form in the lower left corner of the room. The temperature of the absorber plate is maximum and reach to 353.536 K. The time of convert the PCM from solid to liquid is not enough because the thickness of the PCM increased to 5 cm, where the melting fraction (liquid fraction) is equal to 0.992 at time 3 p. m.

Fig. 21 shows the liquid fraction with time for three thickness (t_{PCM})

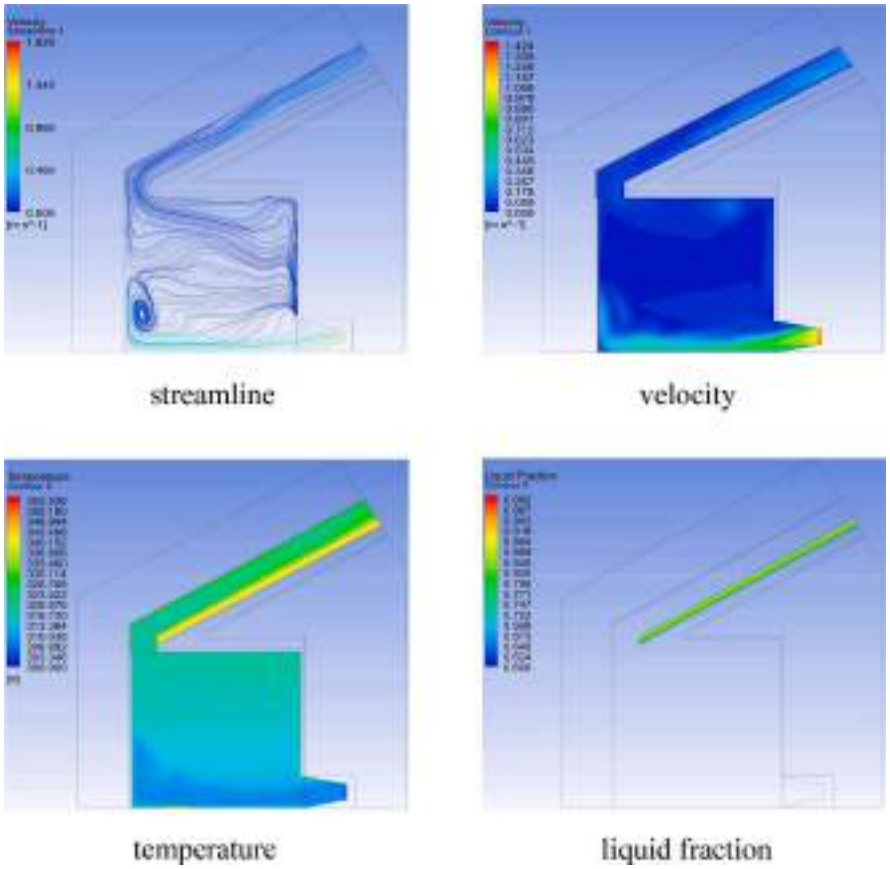

Fig. 20. Contours illustrate the effect of streamline, velocity, temperature distribution, and liquid fraction in the room and solar chimney with PCM at gab = 15 cm, α = 30°, 3 p.m., for basin thickness (t_{PCM} = 5 cm).

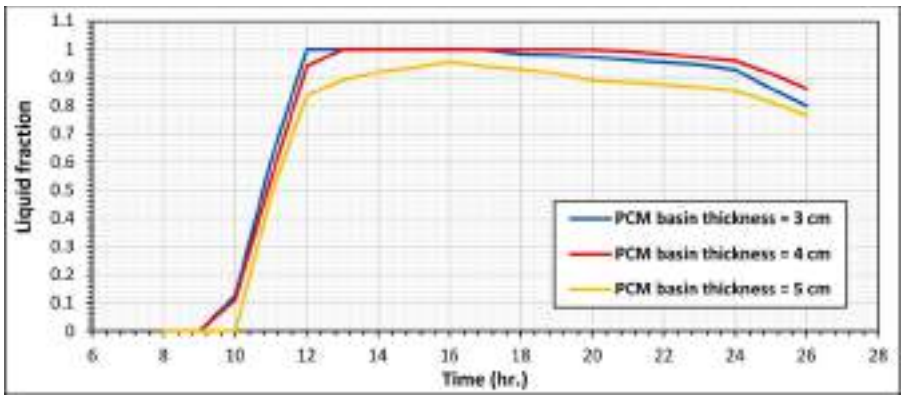

Fig. 21. Liquid fraction with time at gab = 15 cm, α = 30° and different basin thickness of PCM (t_{PCM} = 3 cm, 4 cm, and 5 cm).

= 3 cm, 4 cm, and 5 cm at gab = 15 cm and α = 30° This figure show that the liquid fraction increasing from zero at the morning and becomes 1 after noon due to melt the PCM and then decrease at the night. The thickness of PCM is equal 4 cm gives greater melting fraction along the time compare to another thickness. When the thickness of the PCM tank is 5 cm, the PCM does not melted completely because it needs more time (increase in the amount of solar radiation).

Fig. 22 shows the temperature distribution for the absorber plate with time at gab = 15 cm, α = 30° and different basin thickness of PCM (t_{PCM} = 3 cm, 4 cm, and 5 cm) and without basin of PCM. From the figure, it is evident that in the absence of the PCM basin, the temperature of the heat-absorbing plate initially rises and reaches a peak value of around 351 K at 12 p.m. Subsequently, it starts to release heat and decreases to 309 K by 8 p.m. When phase change material (PCM) is introduced into the solar chimney, there is a noticeable rise in temperature. It reaches its peak at around 352 K at 2 p.m. and the temperature profile are kept almost constant because the charging period of the PCM starts. Subsequently, the temperature gradually decreases, albeit at a slower rate, due to the presence of PCM. Eventually, it reaches a temperature of 328 K at 2 a.m. Additionally, the figure indicates that a PCM thickness of 4 cm results in the maximum temperature and a longer duration of heat retention.

Fig. 23 shows the temperature distribution for PCM with time at gab = 15 cm, α = 30° and different basin thickness of PCM (t_{PCM} = 3 cm, 4 cm, and 5 cm). It can be seen from the figure that the temperature of the PCM increases gradually with time until it reaches the highest value of

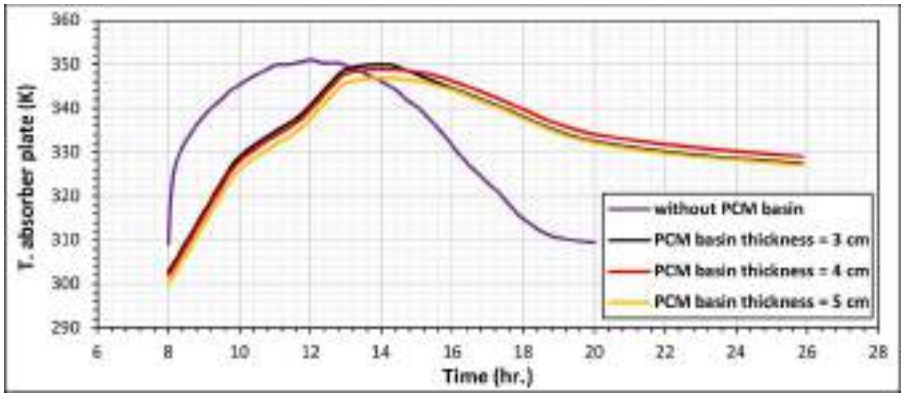

Fig. 22. Temperature distribution for the absorber plate with time at gab = 15 cm, α = 30° and different basin thickness of PCM (t_{PCM} = 3 cm, 4 cm, and 5 cm) and without basin of PCM.

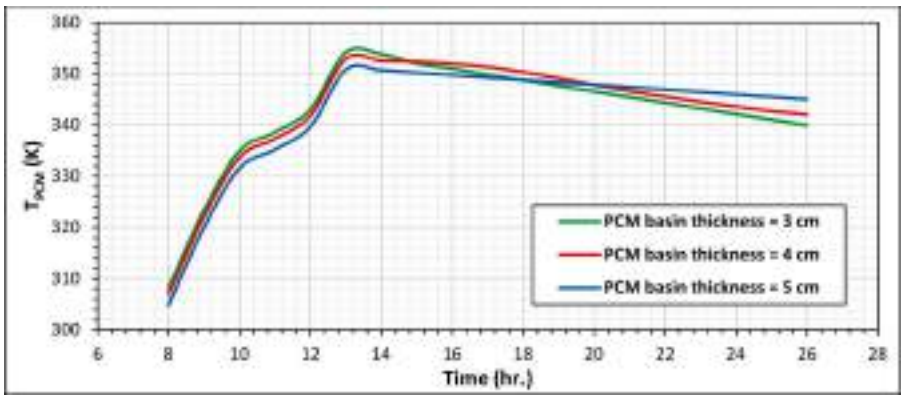

Fig. 23. Temperature distribution for PCM with time at gab = 15 cm, α = 30° and different basin thickness of PCM (t_{PCM} = 3 cm, 4 cm, and 5 cm).

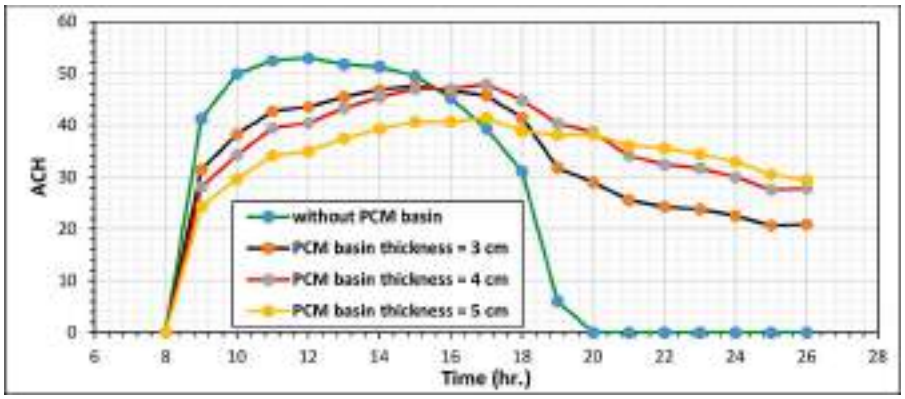

Fig. 24. Air change per hour (ACH) with time at gab = 15 cm, α = 30° and different basin thickness of PCM (t_{PCM} = 3 cm, 4 cm, and 5 cm) and without basin of PCM.

356 K at 1 p. m., after which it begins to decrease. We also notice from the figure that at thickness 4 cm, gives greater temperature of PCM and maintain along the time compare to another thickness.

The variation of ACH with time at gab = 15 cm, α = 30°, and different basin thickness of PCM (t_{PCM} = 3 cm, 4 cm, and 5 cm) and without basin of PCM is shown in the Fig. 24. This figure shows that the maximum ACH along time for thickness 4 cm it reaches about 47 1/h, where the saving energy in the PCM makes the temperature stays high and the buoyancy effect is continuous to the night. Additionally, the chart indicates that in the absence of PCM the maximum ACH reaches about 52.5 1/h at 11 a.m., after that there is a dramatically decline until it reaches zero at 8 p. m., due to the decay of solar radiation and the absence of PCM.

3.2. Experimental results

Fig. 25 shows the ambient temperature with time for two days 30 Sep. 2023 and 15 Oct. 2023. It can be seen that the ambient temperature increases with time from mooring to reach maximum at noon and then decreases to become minimum at the night. Naturally the temperature of September more than temperature of October.

Fig. 26 indicates the solar radiation (W/m^2) with time for two dates, September 30 and October 15 in 2023. This figure shows that the maximum (peaks) solar radiation occurs at noon (12 p. m.) with value

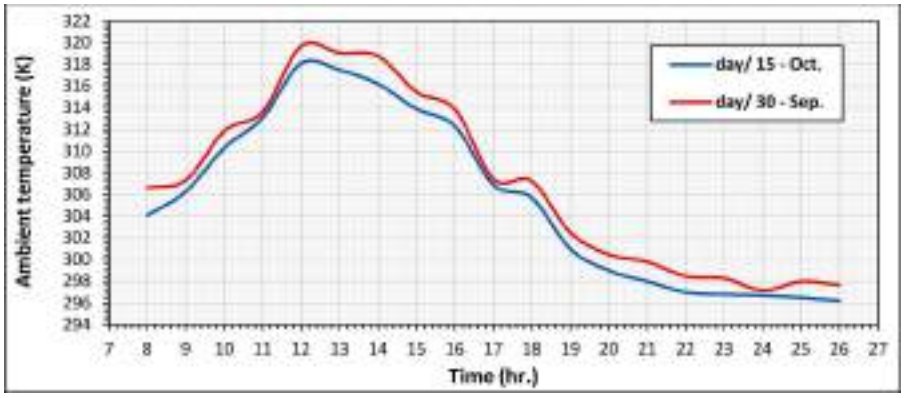

Fig. 25. Ambient temperature with time for days 30 – Sep. 2023 and 15 – Oct 2023.

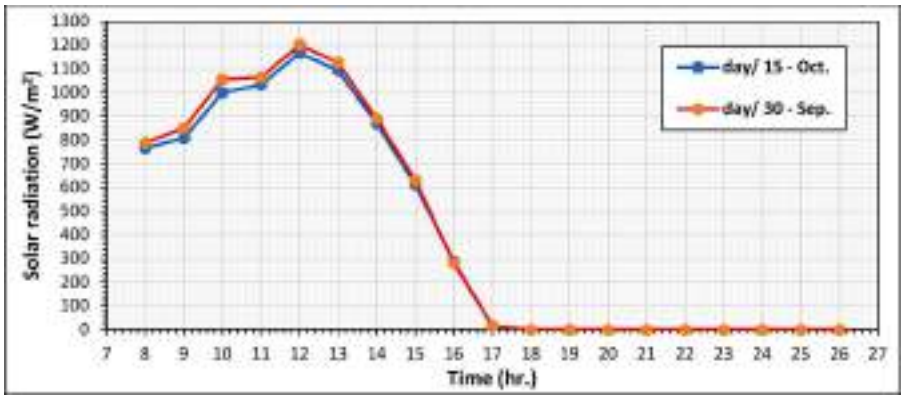

Fig. 26. Solar radiation with time for days 30 – Sep. and 15 – Oct in 2023.

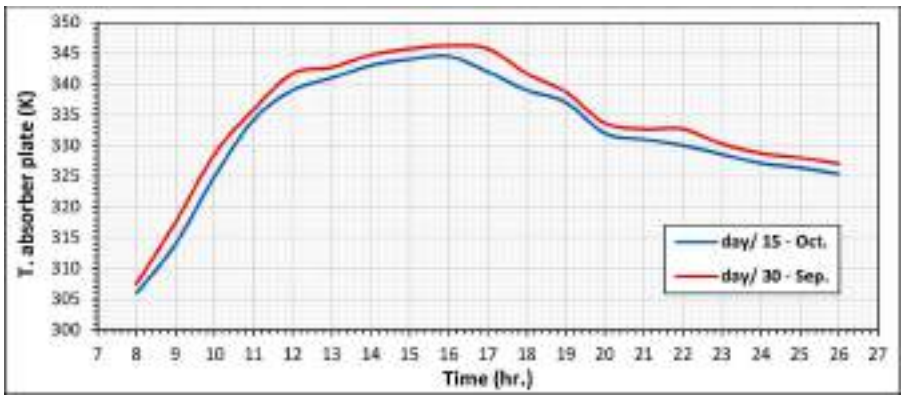

Fig. 27. Temperature distribution for the absorber plate with time at gab = 15 cm, α = 30° and basin thickness (t_{PCM} = 4 cm) for days 30 – Sep. and 15 – Oct. 2023.

1200 W/m^2 approximately and then decreases to reach zero at the night when the sun sets.

Fig. 27 illustrates the variation of the absorber plate average temperature during the operation with time at gab = 15 cm, α = 30°, and t_{PCM} = 4 cm for two days 30 Sep. and 15 Oct. 2023. The temperature of the plate increase with time and become maximum after hour 3 p.m. due to saving energy in the PCM tank and delay in the saving energy. The maximum temperatures are: 347 K, 344.5 K for days 30 Sep. and 15 Oct. respectively. The temperature of the absorber plate stays high at the night, The reason is that, at the night, heat is released from the PCM due to the phase change.

Also, the average temperature of the PCM stays high at the night due to the saving energy at the day. This behavior is shown in the Fig. 28 which shows the variation of the average temperature of PCM with time at gab = 15 cm, α = 30°, and t_{PCM} = 4 cm at days 30 Sep. and 15 Oct. The temperature of PCM becomes more then the melting temperature (340 K) which that the latent heat storage is found, and when the temperature of PCM reaches approximately at the initial solidification temperature the PCM begins to be frozen. From 8 a. m. to 7 p. m. the temperature of the PCM move away from the solid state to reach the liquid state, after that, it begins to solidification slightly because the energy was released by the PCM as sensible heat and the decay of solar radiation at night.

Fig.29 shows the variation of ACH with time at gab = 15 cm, α = 30°, and t_{PCM} = 4 cm for days 30 Spt. and 15 Oct. It can be seen that the ACH becomes maximum at the midday to reach 37 and 34 at days 30 Sep. and 15 Oct. respectively. The ACH on Sep. 30 is greater than the ACH on Oct.

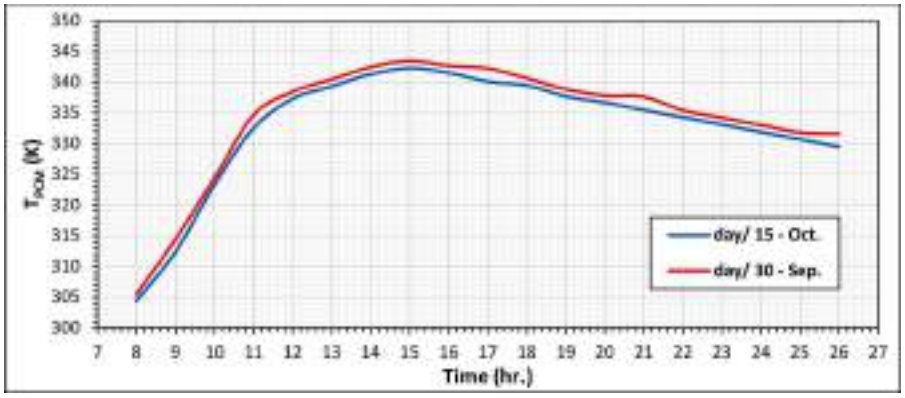

Fig. 28. Temperature distribution for the PCM with time at gab = 15 cm, α = 30° and basin thickness (t_{PCM} = 4 cm) for days 30 – Sep. and 15 – Oct. 2023.

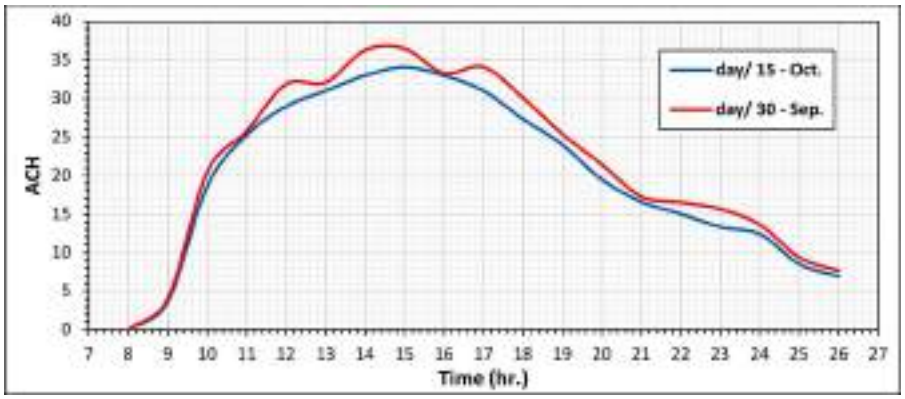

Fig. 29. Variation of air change per hour (ACH) with time at gab = 15 cm, α = 30° and basin thickness (t_{PCM} = 4 cm) for days 30 – Sep. and 15 – Oct. 2023.

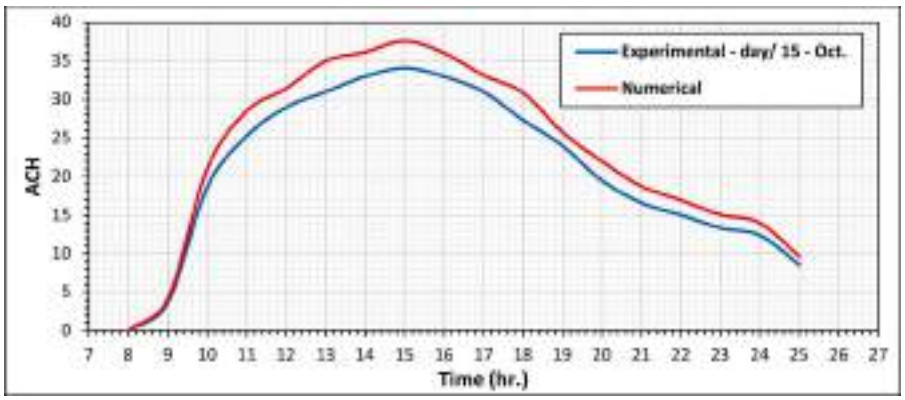

Fig. 30. Comparison between the experimental and numerical results of the ACH variation with daytime at gab = 15 cm, α = 30°, and basin thickness (t_{PCM}) = 4 cm.

15 due to the higher solar radiation on Sep. 30. After that, the ACH it begins to decrease gradually until it becomes 8 at 2 a. m. because the PCM has released the stored heat.

3.3. Comparison

Fig. 30 shows a comparison between experimental and numerical results of ACH with daytime at gab = 15 cm, α = 30°, t_{PCM} = 4 cm and in the day 15 October 2023. It can be seen from the figure that the ACH is increased with day time to reach 37.59 for theoretical and 34.08 for experimental at 3 p. m. and then decreased to reach 9 and 7 for numerical and experimental results at 2 a. m. respectively. The figure acceptable identical between experimental and numerical results with average error 11.597 %.

4. Conclusion

Current research focuses on utilizing solar energy in buildings because it is more environmentally friendly, economically inexpensive, and has longevity and durability. The effect of the solar chimney with the room in the presence and absence of phase change material in the city of Basra, Iraq, was studied theoretically and experimentally, for numerical and theoretical analysis the simulations were conducted using ANSYS - Fluent 2021/R2 and for the experiential the best results that obtained from the numerical simulation in designing was use for built the device and record the data. The effect of several factors and

variables was studied, such as the tilt angles of the solar chimney, the air gap, the addition of a PCM basin to the solar chimney with different thicknesses, the temperature of the heat-absorbing plate, the rate of air change per hour (ACH) in the presence and absence of PCM, and the effect of liquid fraction was studied. The basic results of the current study can be summarized as follows:

1. The solar chimney with the room and without the presence of PCM at the angle $\alpha = 30^{\circ}$ and the air gap = 15 cm gives the almost irregular of the streamlines, and this means to good ventilation (air change per hour) (ACH) was obtained 54.0275 at 12 noon, and leads to better ventilation from angles are $\alpha = 45^{\circ}$ and $\alpha = 60^{\circ}$ for the air gaps of 10 cm and 20 cm. And the maximum average temperature reached at the obserber plate is 350.95 K at 12 noon, which is higher than the angles $\alpha = 45^{\circ}$ and $\alpha = 60^{\circ}$ for the air gaps of 10 cm and 20 cm.
2. When adding a PCM basin of different thickness (t_{PCM} = 3 cm, 4 cm, and 5 cm), it was found that the highest average temperature of absorber plate was 357.861 K at a thickness of 4 cm and at 3 p.m. and a longer heat maintain period occur, and the maximum air velocity was 1.717 m/s. And at basin thickness = 4 cm gives the largest liquid fraction along time, the highest average temperature of PCM, and the best ventilation amount for hourly air change (ACH)
3. In the experimental side, the solar chimney with the room and PCM at angle $\alpha = 30^{\circ}$ and the air gap = 15 cm, in September 30/2023, it was found that the highest average temperature of the obserber plate was 347 K at 3 p.m. The PCM convert into the liquid phase after its melting point, which is 340 K, after 12 noon. After 7 p.m., the PCM begins to solidification slightly, the highest value of air change per hour (ACH) reached 37 at midday due to the increase in the intensity of solar radiation at this time.

CRediT authorship contribution statement

Hussam Hakeem Qasim: Investigation. **Ahmed K. Alshara:** Supervision. **Falah A. Abood:** Supervision.

Declaration of competing interest

The authors declare that they have no known competing financial interests or personal relationships that could have appeared to influence the work reported in this paper.

Data availability

Data will be made available on request.

References

[1] M. Safari, F. Torabi, Improvement of thermal performance of a solar chimney based on a passive solar heating system with phase-change materials, Energy Equipment and Syst. 2 (2) (2014) 141–154.
[2] J. Li, X. Gao, Y. Li, Thermal storage capacity and night ventilation performance of a solar chimney combined with different PCMs, Int. J. Photoenergy 2017 (4) (2017) 1–10.
[3] J.C.F. Dordelly, M.C.M. El Mankibi, R.E.M. Miranda, M. Jimenez, J.A. Landa, Numerical and experimental assessment of a PCM integrated solar chimney, Int. J. Energy Environ. Eng. 12 (4) (2018) 252–258.
[4] B. Buonomo, L. Capasso, A. Diana, O. Oronzio Manca, S. Nardini, A numerical analysis on a solar chimney with an integrated latent heat thermal energy storage, AIP Conf. Proc. 2191 (2019) 020029–1–020029-10.
[5] S.M. Salih, S.E. Najim, J.M. Jalil, Numerical modeling for novel solar air heater utilizing wax paraffin-PCM, Bas J Eng. Sci. 19 (2) (2019) 1–8.
[6] S.K. Nateghi, M.H. Jahangir, Performance evaluation of solar chimneys in providing the thermal comfort range of the building using phase change materials, Clean. Mater. 5 (100120) (2022) 44–100.
[7] H.H. Naser, S.H. Hammadi, Effect of phase change material and roof shading on cooling load of residential unit in basrah, Bas J Eng. Sci. 22 (2) (2022) 33–40.
[8] T. Abduljabbar, A.J. Jubear, B.M. Faisal, Numerical study of improving solar chimney performance by using energy storage, Wasit J. Eng. Sci. 10 (3) (2022) 42–57.
[9] D. Qin, J. Liu, G. Zhang, A novel solar-geothermal system integrated with earth-to-air heat exchanger and solar air heater with phase change material-numerical modelling, experimental calibration and parametrical analysis, J. Build. Eng. 35 (2021) 101971.
[10] M.E. Tiji, R. Yousefzadeh, M. Eisapour, M. Azadian, P. Talebizadehsardari, A numerical study of a PCM-based passive solar chimney with a finned absorber, J. Build. Eng. 32 (2020) 101516.
[11] Q. Liu, Y. Huang, Y. Maa, Y. Peng, Y. Wang, Parametric study on the thermal performance of phase change material-assisted earth-to-air heat exchanger, Energy Build. 238 (2021) 110811.
[12] T. Long, Y. Li, S. Shuli Liu, J. Jun lu, Benefits of integrating phase-change material with solar chimney and earth-to-air heat exchanger system for passive ventilation and cooling in summer, Energy Storage 48 (2022) 104037.
[13] V.M. Maytorena, J.F. Hinojosa, S. Moreno, D.A. Buentello-Montoya, Thermal performance analysis of a passive hybrid earth-to-air heat exchanger for cooling rooms at Mexican desert climate, Case Stud. Therm. Eng. 41 (2023) 102590.
[14] P. Thantong, J. khedari, P. Chantawong, Investigation of thermal performance by applying a solar chimney with PCM towards the natural ventilation of model house under climate of Thailand, Mater. Today 5 (2018) 14862–14867.
[15] N. Fadaei, A. Kasaeian, A. Akbarzadeh, S.H. Hashemabadi, Experimental investigation of solar chimney with phase change material (PCM), Renew. Energy 132 (2018) 26–35.
[16] D.M. Hachim, Q.A. Abed, V. Badescu, Performance of double pass unglazed transpired collectors with energy storage in phase change materials during days with different radiative regimes, Sustain. Energy Technol. Assess. 46 (2021) 101309.
[17] H.K. Versteeg, W. Malalasekera W., An Introduction to Computational Fluid Dynamics, 2007. London. England.
[18] A. Pasupathy, L. Athanasius, R. Velraj, R.V. Seeniraj, Experimental investigation and numerical simulation analysis on the thermal performance of a building roof incorporating phase change material (PCM) for thermal management, Appl. Therm. Eng. 28 (2008) 556–565.
[19] B. Buonomo, D. Ercole, O. Manca, S. Nardini, Thermal behaviors of latent thermal energy storage system with PCM and aluminum foam, Int. J. Heat Technol. 34 (2) (2016) S359–S364.
[20] A. Saraswat, A. Verma, S. Khandekar, M.K. Das, Latent heat thermal energy storage in a heated semi-cylindrical cavity: experimental results and numerical validation, in: Proceedings of the 23rd National Heat and Mass Transfer Conference and 1st International ISHMT-ASTFE Heat and Mass Transfer Conference IHMTC2015, 2015.
[21] A.D. Korawan, S. Soeparman, W. Wijayanti, D. Widhiyanuriyawan, 3D numerical and experimental study on paraffin wax melting in thermal storage for the nozzle-and-shell, tube-and-shell, and reducer-and-shell models, Model. Simul. Eng. 2017 (2) (2017) 1–9.
[22] K. Nithyanandam, R. Pitchumani, Optimization of an encapsulated phase change material thermal energy storage system, Solar Energy 107 (2014) 770–788.
[23] j. Soibam, Numerical Investigation of a Heat Exchanger using Phase Change Materials (PCMs), Norwegian University of Science and Technology, Norway, 2018. Thesis for: Master Degree.
[24] V.R. Voller, C. Prakash, A fixed grid numerical modelling methodology for convection-diffusion mushy region phase-change problems, Int. J. Heat Mass Transfer 30 (8) (1987) 1709–1719.
[25] A. Hesaraki, CFD Modeling of Heat Charging Process in a Direct-Contact Container for Mobilized Thermal Energy Storage, Malardalen University Sweden, 2011.
[26] Y.H. Qian, S.A. Orsag, Lattice BGK models for the Navier-Stokes equation: nonlinear deviation in Compressible Regimes, Europhys Lett 21 (3) (1993) 255–259.
[27] ANSYS CFX-Solver Theory Guide, ANSYS CFX Release 11.0", 2006. U.S.A.
[28] A.M. Salman, A.A. Monem, E.A. Khazal, Indoor air quality in a cardiac care unit (CCU) under different ventilations, Bas. J. Eng. Sci. 21 (1) (2021) 1–7.
[29] Z. Shi, J. Chen, Q. Chen, On the turbulence models and turbulent Schmidt number in simulating stratified flows, J. Build. Perform. Simul. 9 (2) (2015) 134–148.
[30] H.B. Awbi, Ventilation of Buildings, 2003. LondonISBN 0-203-63447-0 Master e-book ISBN.
[31] J.F. Thompson, B. Bharat Soni, N. Weatherill, Handbook of Grid Generation, CRC Press, BacoRaton, London, NewYork, Washington D.C., 1999.
[32] R. Bassiouny, N.S.A. Koura, An analytical and numerical study of solar chimney use for room natural ventilation, Energy Build. 40 (5) (2008) 865–873.
[33] J. Mathur, N.K. Bansal, S. Mathur, M. Jain, Anupma, Experimental investigations on solar chimney for room ventilation, Solar Energy 80 (8) (2006) 927–935.
[34] D. Park, The Application of the Solar Chimney for Ventilating Buildings, 2016. Ph D thesisVirginia.